Journal of Materials Research and Technology 40 (2026) 2820–2832

Contents lists available at ScienceDirect

Journal of Materials Research and Technology

journal homepage: www.elsevier.com/locate/jmrt

Nucleation control strategy for sustainable aluminium: Improving Fe removal efficiency or increasing Fe-tolerance

Zhongping Que *, Zhongyun Fan

Brunel Centre for Advanced Solidification Technology (BCAST), Brunel University London, Uxbridge, Middlesex, UB8 3PH, UK

ARTICLE INFO

Keywords:
Heterogeneous nucleation
Fe-containing intermetallic compounds
Fe removal
Refinement
Al–Fe–Mn–Mg–Si

ABSTRACT

Achieving ultra-low Fe level or refining Fe-containing intermetallic compounds (Fe-IMCs), both governed by heterogeneous nucleation, remains a major challenge for development of high-performance recycled Al alloys. This study demonstrates that the sensitivity of Fe-IMC formation to casting conditions is dictated by nucleation difficulty, which is controlled by both kinetic factors (diffusion time) and thermodynamic driving forces (nucleation and continuous undercooling). We provide the first direct evidence for dual-size primary Fe-IMCs and their distinct nucleation pathways: large P1-α-$Al_{15}(Fe,Mn)_3Si_2$ particles originating from non-equilibrium θ-$Al_{13}Fe_4$ nucleated at higher temperatures, and nanoscale P2-α-Fe particles nucleating heterogeneously on $MgAl_2O_4$ oxides at lower temperatures with larger nucleation undercooling. Building on this new mechanistic understanding, two casting strategies were developed: (1) promoting Fe-IMC nucleation to enhance Fe removal down to 0.3 wt%, and (2) suppressing Fe-IMC formation to increase Fe tolerance and refine second-phase particles, enabled by tuning pouring temperature, cooling rate, and casting routes. A comprehensive process map linking Fe-IMC formation to cooling rate and pouring temperature is established, providing a predictive framework for process optimization. These insights position nucleation-control-based design as a powerful approach for sustainable aluminium production.

1. Introduction

Addressing the urgent global challenge of decoupling economic growth from environmental degradation, with metals playing a critical role. Aluminium stands out due to its strength, light weight, and exceptional recyclability. Current aluminium sector remains heavily dependent on energy-intensive primary production, which is environmentally unsustainable and risks undermining net-zero ambitions [1,2]. Unlocking aluminium's full circular potential through advanced recycling is vital to reducing carbon emissions, conserving resources, and securing supply chains worldwide. However, the transition to high-quality secondary aluminium is constrained by persistent technical barriers, particularly the challenge of managing impurities and non-metallic inclusions in scrap.

Although various technologies have been developed to address the challenges posed by non-metallic inclusions [3–5], developing effective methods to control impurities remains a significant challenge [6–8]. In aluminium recycling, impurities refer to unwanted elements that contaminated aluminium scrap and dissolve into the liquid aluminium during remelting process, thereby degrading the quality of the recycled metal. Some elements, such as Fe, are typically considered unwanted alloying elements in recycled aluminium, as they can easily exceed the tolerance limits specified for primary aluminium alloys [7–9]. Interestingly, these elements are also commonly used as major (> 1.0 wt.%) or minor (<1.0 wt.% and > 0.1 wt.%) alloying constituents in designed Al alloys, meaning that their classification as impurities depends largely on concentration specification [10]. In recycled Al alloys, excessive levels of these elements often lead to the formation of primary intermetallic compounds (P-IMCs) or secondary phase particles (SPPs) [11,12], depending on their solubility and accumulated concentration in aluminium. A deep understanding of formation mechanisms of these P-IMCs and SPPs requires long-term scientific investigation, which in turn has delayed the development of effective technologies to mitigate impurity-related issues.

Among these, iron (Fe) is one of the most critical impurities which is most difficult to control and tackle, limiting the quality of recycled aluminium. The difficulties are related to following aspects.

* Corresponding author.
E-mail address: Zhongping.Que@brunel.ac.uk (Z. Que).

https://doi.org/10.1016/j.jmrt.2026.01.034
Received 18 November 2025; Received in revised form 2 January 2026; Accepted 5 January 2026
Available online 6 January 2026

(1) Extreme low solubility in Al [13]: Fe has very small solubility in aluminium at room temperature, which therefore majority Fe concentration has to be solidified as P-IMCs or SPPs after solidification.
(2) Nucleation difficulty: nucleation of Fe-IMCs requires multiple types of alloying elements occupy different atomic positions which required large energy/nucleation undercooling. The nucleation of Fe-IMCs additional requires so-called compositional templating [14].
(3) Slow diffusion rate: Fe, as the main constituent element in Fe-IMCs, exhibits a very low diffusion rate in aluminium [15]. This sluggish atomic mobility hinders the redistribution of Fe atoms during solidification, thereby reducing the likelihood of achieving the local supersaturation needed for heterogeneous nucleation. As a result, the nucleation of Fe-IMCs becomes energetically difficult, and their formation is often delayed until the late stages of solidification.
(4) Rapid growth speed of Fe-IMCs in binary eutectic (BE) [16]: as the results of the nucleation difficulty, early-stage formation of Fe-IMCs are normally be suppressed, which providing the supersaturated and large driving force for the formation of the next stage formation as second phase particles. Growth can then proceed rapidly once favourable conditions are established. The extreme low solubility of Fe facilitates the Fe rejected into the Al inter-dendritic zone also provides the favourable solute supply for the rapid growth.

The large size of Fe-IMCs degrades mechanical performance and reduce the potential for high-quality recycling. Addressing Fe impurities is therefore essential for sustainable aluminium production and a circular metals economy. Traditional approaches to Fe management in aluminium alloys include the removal of Fe and the refinement of Fe-IMCs. Sedimentation is one of the most common Fe removal methods [17,18], but conventional techniques without melt treatment are limited by nucleation difficulties, typically capping Fe removal at around 0.7 wt %. Enhancing heterogeneous nucleation to promote the formation of primary Fe-IMCs is therefore crucial. This can be achieved through alloying i.e. Mn, Cr, Co [17,18] or process adjustments, transforming needle-like morphologies into more compact forms that can be more easily removed from the melt. Progress in this area has been slow due to limited understanding of Fe-IMC formation mechanisms. Over the past decades, our research group has focused on elucidating these nucleation mechanisms and developing technologies to refine Fe-IMCs, including insights such as compositional templating [14].

Another approach to managing Fe impurity is to control the large Fe-IMCs that solidify as second-phase particles (SPPs) within eutectic structures. Refining Fe-IMCs by controlling their size, shape, and distribution, is a key strategy to increase Fe tolerance without compromising alloy performance. Techniques include chemical modification (e.g., Mn or Cr addition), high-strain deformation, and heat treatment. While advanced methods such as powder metallurgy, 3D printing, laser processing, and rapid solidification can produce finer Fe-IMCs, they are not yet practical for large-scale industrial processes like direct-chill (DC) casting.

Our research group focused on the complex and casting-sensitive phase selection of Fe-rich intermetallic compounds in an Al–5Mg–2Si-0.7Mn-1.2Fe alloy over the years, addressing long-standing challenge in their control. Building on our systematic studies, which combined advanced characterization techniques (SEM, EBSD, TEM) with thermodynamic and density functional theory (DFT) analyses, we have progressively clarified the nucleation mechanisms and phase-selection behaviour of Fe-IMCs that were previously unresolved. Our earlier work [19] firstly demonstrated the competitive nucleation between θ-$Al_{13}Fe_4$ and α-$Al_{15}(Fe,Mn)_3Si_2$, followed by the identification of a more complex three-phase nucleation competition involving θ-$Al_{13}Fe_4$, $Al_6(Fe,Mn)$, and α-$Al_{15}(Fe,Mn)_3Si_2$ [20]. Based on these mechanistic insights, this study advances the field by establishing a nucleation-control strategy for sustainable aluminium processing. Specifically, we provide direct evidence for dual-size primary Fe-IMCs with distinct nucleation mechanisms, develop a processing design that markedly enhances Fe-removal efficiency (from 0.7 wt% down to 0.3 wt%), and construct the first comprehensive map linking cooling rate and pouring temperature to the enhancement or suppression of Fe-IMC formation. This work bridges fundamental nucleation theory with practical process implementation and, for the first time, demonstrates that targeted control of nucleation pathway can directly enable effective Fe purification and improved Fe tolerance in recycled aluminium system.

2. Experimental

2.1. Alloys preparation and casting

The alloy investigated in this work was designed with a nominal composition of Al–5Mg–2Si-0.7Mn-1.2Fe, and the actual measured composition was 5.1 Mg, 2.2 Si, 0.69 Mn, and 1.18 Fe (wt.%), with the balance being Al. The phase diagram of this alloy was calculated using the Pandat software under both Scheil [21] and equilibrium conditions, and the results are summarized in Table 1. The alloy was prepared using commercial-purity (CP) Al (99.9 wt%), CP Mg (>99.95 wt%), and various master alloys, including Al–50 wt% Si, Al–20 wt% Mn, and Al–38 wt% Fe. To compensate for the vaporization of volatile elements such as Mg during melting, an additional 5 wt% CP-Mg was introduced, ensuring that the final chemical composition closely matched the nominal design. The CP-Al and all master alloys were first melted at 750 °C in an electric resistance furnace, followed by thorough stirring to ensure complete dissolution. The CP-Mg was wrapped in Al foil, preheated to 200 °C, and then added into the melt. After the complete dissolution of Mg, the melt was held for an additional 30 min before further processing.

The alloy melt was cast under different conditions, which are summarized in Table 2. Casting was performed using a Tp-1 mould [22], specifically designed to provide a cooling rate of ~3.5 K/s at a location of 38 mm from the bottom of the casting, thereby replicating the conditions of industrial direct-chill (DC) casting. The Tp-1 mould was preheated to 380 °C prior to use. For casting experiment with pouring temperatures below 750 °C, the melt was air-cooled with stirring, yielding an average cooling rate of ~1 K/s, as determined from the cooling time and temperature difference. To achieve a much slower cooling rate of ~0.02 K/s, the melt was transferred into small crucible and cooled inside a furnace programmed at 750 °C.

To investigate the heterogeneous nucleation of Fe-IMCs, pressured-filter equipment was employed to collect native oxides and inclusions through a ceramic filter with a 40 μm mesh from a 2 kg melt. The process was conducted under an argon gas pressure of 58 psi(~4 bar). The crucible, fitted with the filter at the bottom, was preheated using a resistance wire heater for 3–4 h (approximately 800 °C). The pouring temperature was raised to 800 °C to minimize heat loss and ensure that at least 60 % of the melt passed through the filter before solidification occurred. To examine the effects of cooling rate on Fe-IMC formation, the alloy was also processed via suction casting under an argon atmosphere, achieving a cooling rate of approximately 40 K/s.

Table 1
Thermodynamic calculation results of studied alloy.

	liquidus (°C)	T_{fcc} (°C)	f(α) before T_{fcc}	Fe wt.% in liquid before T_{fcc}
Scheil	668.0	620.5	2.78 %	0.7456
Equilibrium	671.0	620.8	2.87 %	0.696

Table 2
Casting conditions and experimental result in this study.

	T1-T2 (°C)	Cooling rate K/s	T2-T3 (°C)	Cooling rate K/s	T3-T4 (°C)	Cooling rate K/s	Experimental result
1	720–20	3.5	–	–	–	–	A few θ→α (P1), suppressed P–Fe, large size BE-Fe
2	750–700	1 (AC)	700–20	3.5	–	–	Multiple types of metastable Fe-IMCs, large size BE-Fe
3	750–670	1	670–20	3.5	–	–	A few θ→α (P1), suppressed P–Fe, large size BE-Fe
4	750–650	1	650–20	3.5	–	–	More P1–Fe and some P2(Fe)
5	750–630	1	630–20	3.5	–	–	Explosive and refined P1–Fe, little BE-Fe
6	750–620	1	620–20	3.5	–	–	Barely P–Fe and BE-Fe, mostly ME-Fe
7	750–630	1	630-670 (heat up)	0.05	670–20	3.5	Explosive and refined P1–Fe, little BE-Fe
8	750–20	0.02	–	–	–	–	A few settled P1–Fe IMCs
9	750–630	1	630-670(heat up)	0.05	670–20	0.02	Many small P–Fe
10	720–20	40	–	–	–	–	No P–Fe and BE-Fe, ME-Fe

Note: P represents primary; BE represents binary eutectic; ME represents multiple component eutectic.

2.2. Characterization

Samples from different casting conditions were prepared according to standard procedures, including sectioning, mounting, sandpaper polishing, and final OPS polishing. The microstructure was initially examined using a Zeiss optical microscope equipped with AxioVision 4.3 image analysis software. The size measurement of large-scale P1-αFe was conducted using 15 particles across the entire sample, due to the limited particle number density. In contrast, the size measurement of P2-αFe was based on at least 50 particles. The compositional analysis of all particles in this study was performed using a minimum of 10 measurement points per particle. EBSD and SEM investigations were conducted on a Zeiss Crossbeam 340 FIB-SEM operated at an accelerating voltage of 20 kV. The EBSD scanning step size was set between 0.1 and 0.2 μm.

To investigate the heterogeneous nucleation of Fe-IMCs, thin foils were extracted from 0.5 mm above the filter and prepared for transmission electron microscopy (TEM). The foils were mechanically ground to a thickness of ~100 μm, cut into 3 mm diameter discs, and further thinned to approximately 60 μm. Final polishing was carried out using ion-beam thinning with a Gatan precision ion polishing system (PIPS) operated at 2.0–5.0 kV and an incident angle of 3–5°. TEM analysis was performed on a JEOL 2100F transmission electron microscope equipped with an EDX spectrometer, operated at an accelerating voltage of 200 kV.

To examine the three-dimensional (3D) morphology of intermetallic compounds, as-cast samples were deep-etched in a 15 % HCl solution for 2–3 min, followed by immersion in a methanol bath. The complex 3D morphology of the Fe-IMCs, including other types of Fe-IMCs embedded within the particles, was characterized using a Zeiss Xradia 410 Versa X-ray microscope operated at 80 kV and 10 W.

3. Results

3.1. Nucleation difficulty of Fe-IMCs

The thermodynamic calculations of the Al–5Mg–2Si-0.7Mn-1.2Fe

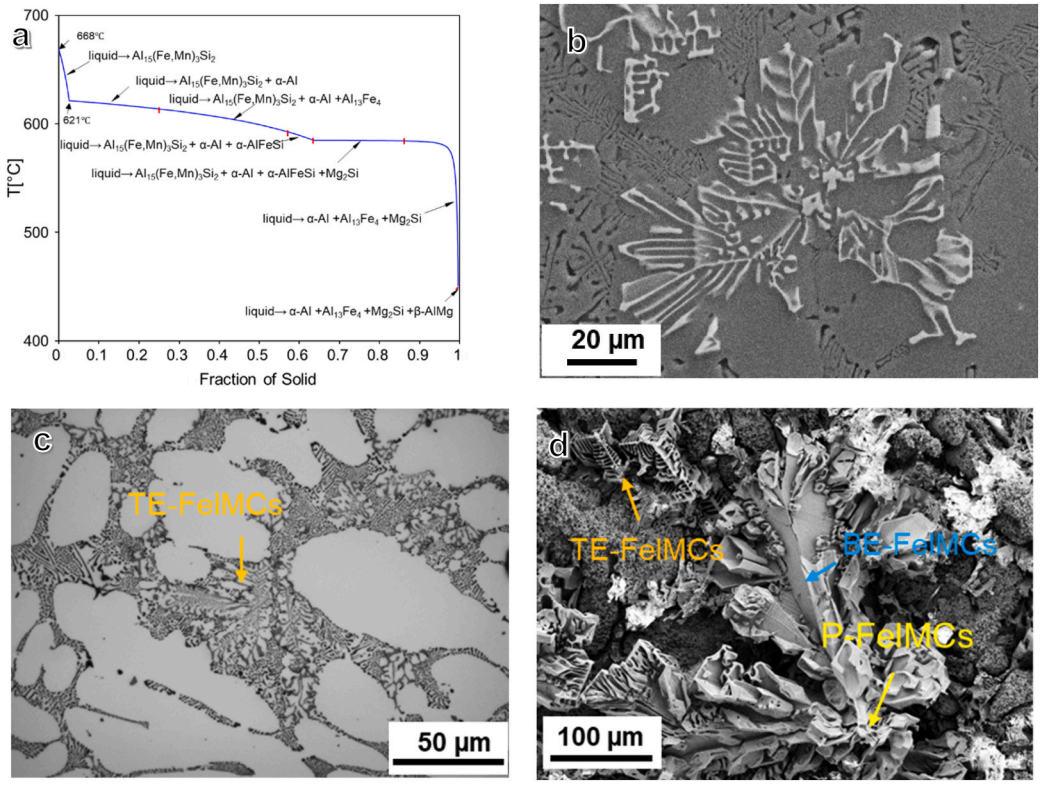

Fig. 1. Solidification behaviour and as-cast microstructure of Al–5Mg–2Si-0.7Mn-1.2Fe. (a) Calculated solidification curve under the Scheil model; (b) SEM image of the as-cast microstructure at 3.5 K/s from 720 °C, showing primary Fe-IMCs, Chinese-script Fe-IMCs, and Mg_2Si in eutectic structures; (c) Optical image highlighting Chinese-script Fe-IMCs in the ternary eutectic structure; (d) SEM image of deep-etched sample showing the morphology of Fe-IMCs in primary, binary, and ternary eutectic structures.

alloy using both Scheil and equilibrium models are summarized in Table 1. The results indicate the liquidus temperature of 668 °C (Scheil) or 671 °C (equilibrium) with different models, while the temperature for complete solidification of the maximum Al phase (T_{fcc}) is 620.5 °C under the Scheil model and 620.8 °C under the equilibrium model. As shown in the solidification curve calculated with the Scheil model (Fig. 1a), the primary phase to solidify is α-$Al_{15}(Fe,Mn)_3Si_2$, giving a solidification range of approximately 50 °C for the primary Fe-IMCs. The calculated volume fraction of primary α-$Al_{15}(Fe,Mn)_3Si_2$ is 2.78 % under the Scheil model and 2.87 % under the equilibrium model. Correspondingly, the remaining Fe concentration in the liquid before the formation of α-Al is 0.7456 % and 0.696 % (wt.%, unless otherwise specified) for the Scheil and equilibrium models, respectively. The differences between the two models are relatively small when compared with the experimental casting.

Fig. 1 illustrates the solidification behaviour and microstructural features of the Al–5Mg–2Si-0.7Mn-1.2Fe alloy under different observations. The calculated solidification curve obtained from the Scheil model (Fig. 1a) reveals the major solidification sequence as:

1. α-$Al_{15}(Fe,Mn)_3Si_2$;
2. α-$Al_{15}(Fe,Mn)_3Si_2$ + α-Al;
3. α-$Al_{15}(Fe,Mn)_3Si_2$ + α-Al + $Al_{13}Fe_4$;
4. α-$Al_{15}(Fe,Mn)_3Si_2$ + α-Al + α-Al_8Fe_2Si.
5. α-$Al_{15}(Fe,Mn)_3Si_2$ + α-Al + α-Al_8Fe_2Si + Mg_2Si.
6. α-Al +θ-$Al_{13}Fe_4$ + Mg_2Si.

The as-cast microstructure shown in Fig. 1b–d, solidified at a cooling rate of 3.5 K/s from 720 °C reflects the major solidification sequence predicted by the calculated Scheil model. The microstructure contains primary Fe-intermetallic compounds (Fe-IMCs), Chinese-script Fe-IMCs and Mg_2Si within the eutectic regions. Fig. 1b shows primary Fe-IMC particles associated with Chinese script Fe-IMCs, which have been identified as primary α-$Al_{15}(Fe,Mn)_3Si_2$ nucleating BE-α-$Al_{15}(Fe,Mn)_3Si_2$ [19]. Fig. 1c focuses on the last solidified area, containing black Mg_2Si alongside Chinese script α-$Al_{15}(Fe,Mn)_3Si_2$ and α-Al. The deep-etched 3-dimensional (3D) morphology shown in Fig. 1d captures the complete microstructure, clearly illustrating the solidification sequence as.

1. α-$Al_{15}(Fe,Mn)_3Si_2$;
2. α-$Al_{15}(Fe,Mn)_3Si_2$ + α-Al;
3. α-$Al_{15}(Fe,Mn)_3Si_2$ + α-Al + Mg_2Si.

However, the measured volume fraction of primary Fe-IMC particles (Table 3) is only 0.29 %, which is significantly lower than the calculated values of 2.78 % and 2.87 % under the same casting conditions. The remaining Fe in the liquid before α-Al solidification is 2.32 %, which subsequently solidified as eutectic Fe-IMCs. This high Fe content remained in the liquid contributes to the formation of relatively larger secondary Fe-IMC particles with higher volume fraction. These results demonstrate the nucleation difficulty of the Fe-IMCs.

Table 3
Experimental quantified and calculated volume fractions of Fe-IMCs and Fe concentrations in different structures.

	Volume fraction (*f*) of P1	*f* (P2)	Calculated Fe wt.% remain in liquid before T_{fcc}	*f* (P1+P2)	*f* (BE-Fe)	*f* (P + BE)-Fe
5#: 750–630, TP1	1.75	3.81	0.365	5.56	2.19	7.75
1#: 720–20, Tp1	0.29	0	2.32	0.29	7.03	7.32
Scheil	2.78		0.7456	2.78	0.38	3.16
Equilibrium	2.87		0.696	2.87	2.06	4.93

3.2. Suppression of Fe-IMC formation

An interesting phenomenon was observed regarding the suppression of primary equilibrium α-$Al_{15}(Fe,Mn)_3Si_2$ and the phase competition among Fe-IMCs and the overgrown BE-Fe-IMCs, which are sensitive to the pouring temperature. Fig. 2 illustrates the variation of primary Fe-IMCs at different pouring temperatures (720, 700, and 670 °C, above the liquidus) with a cooling rate of 3.5 K/s. Fig. 2a and b shows that at 720 °C, only a few primary α-$Al_{15}(Fe,Mn)_3Si_2$ particles are present, nucleating the surrounding Chinese-script eutectic α-$Al_{15}(Fe,Mn)_3Si_2$ These primary α-$Al_{15}(Fe,Mn)_3Si_2$ particles are not formed via direct nucleation but rather by phase transformation from pre-solidified θ-$Al_{13}Fe_4$ particles, as reported previously [19]. A more complex phase competition occurs when the alloy is cast from 700 °C (Fig. 2c and d), where multiple types of Fe-IMCs, including θ-$Al_{13}Fe_4$, α-$Al_{15}(Fe,Mn)_3Si_2$ and $Al_6(Fe,Mn)$, coexist due to nucleation competition [20]. At a lower pouring temperature of 670 °C, close to the liquidus, non-equilibrium primary Fe-IMCs are not observed; however, a few large primary α-$Al_{15}(Fe,Mn)_3Si_2$ particles form, surrounded by eutectic Chinese-script α-$Al_{15}(Fe,Mn)_3Si_2$. These large particles, approximately 50 ± 5 μm in size, are designated as P1-αFe.

This study also revealed that, in addition to pouring temperature, the formation of Fe-IMCs is highly sensitive to the cooling rate. Fig. 3 illustrates the effect of rapid solidification on the Al–5Mg–2Si-0.7Mn-1.2Fe alloy, cast at a cooling rate of 40 K/s from 720 °C. The optical images show that rapid solidification effectively suppresses the formation of both primary and BE-Fe-IMCs. At low magnification (Fig. 3a), the microstructure is dominated by primary α-Al and eutectic structures, with minimal primary Fe-IMCs. At higher magnification (Fig. 3b), elongated primary α-Al dendrites are observed, surrounded by inter-dendritic zones containing fine secondary phase particles (SPPs), including Fe-IMCs and Mg_2Si. These observations demonstrate that rapid cooling refines the microstructure and limits the size and quantity of Fe-containing intermetallic. The results highlight the critical role of diffusion as a kinetic driving force for Fe-IMC nucleation: at ultra-fast cooling rates, there is insufficient time for atoms to diffuse and form the composition templates required for Fe-IMC nucleation [14], leading to their suppression.

Fig. 4 illustrates the effect of casting slightly below the eutectic temperature on the Al–5Mg–2Si-0.7Mn-1.2Fe alloy, solidified at 3.5 K/s and 620 °C (just below the eutectic point of 620.5 °C). The as-cast microstructure (Fig. 4a) is dominated by primary α-Al and inter-dendritic secondary phase particles (SPPs), with Fe-IMCs exhibiting Chinese-script morphologies ranging from 50 to 200 μm in their longest dimension. Smaller α-Al grains (~200 μm) are surrounded by inter-dendritic Fe-IMCs and Mg_2Si particles, as shown in Fig. 4b. Higher-magnification imaging (Fig. 4c) reveals the fine Chinese-script structures of both Fe-IMCs and Mg_2Si, with average spacings of 5.5 ± 1 μm and 1.6 ± 0.4 μm, respectively. Rare primary Fe-IMCs are also observed within α-Al grains (Fig. 4d), often associated with needle- or plate-like β-Fe-IMCs, as well as some ternary Fe-IMCs connected to nearby Mg_2Si particles. These observations indicate that lowering the pouring temperature slightly below the eutectic point suppresses the formation of large primary Fe-IMCs while promoting fine inter-dendritic Fe-containing phases. It also reveals the competition between all types of Fe-IMCs and α-Al during solidification.

3.3. Stimulated nucleation and formation of primary α-Fe

Fig. 5 illustrates the stimulated nucleation of Fe-IMCs when the Al–5Mg–2Si-0.7Mn-1.2Fe alloy is poured at temperatures lower than the liquidus but higher than the eutectic point ($T_E < T_p < T_L$), with a cooling rate of 3.5 K/s. At 650 °C, the as-cast microstructure (Fig. 5a–c) shows an increased number of primary Fe-IMC particles, ranging from 15 to 30

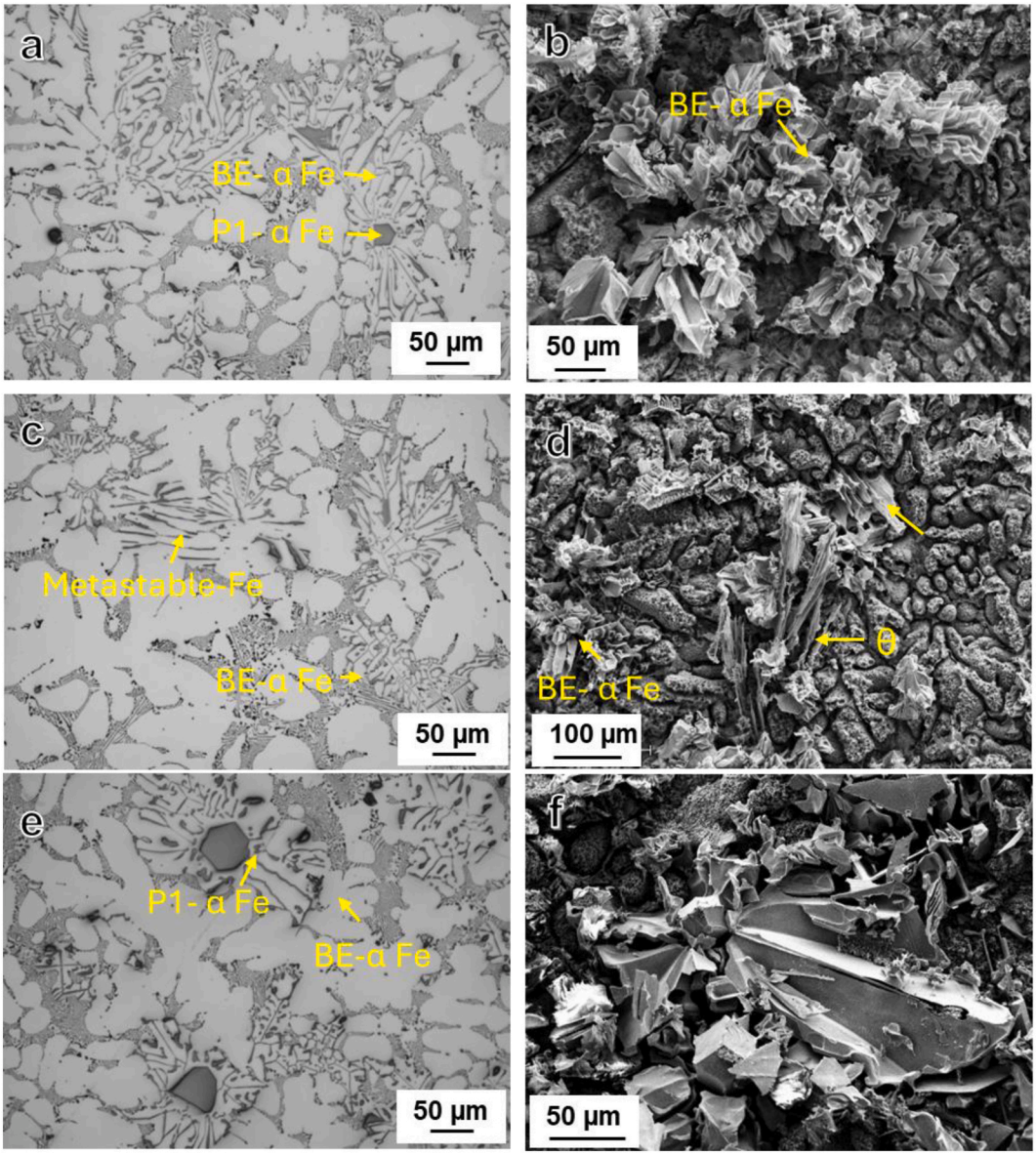

Fig. 2. Suppression of primary Fe-IMCs and overgrown binary-eutectic (BE) Fe-IMCs. Optical (a, c, e) and SEM-BSD (b, d, f) images showing the as-cast microstructure of Al–5Mg–2Si-0.7Mn-1.2Fe alloy in 2D and 3D, cast at 3.5 K/s from: (a, b) 720 °C (>liquidus, Condition 1#); (c, d) 700 °C (>liquidus, Condition 2#); (e, f) 670 °C (>liquidus, Condition 3#).

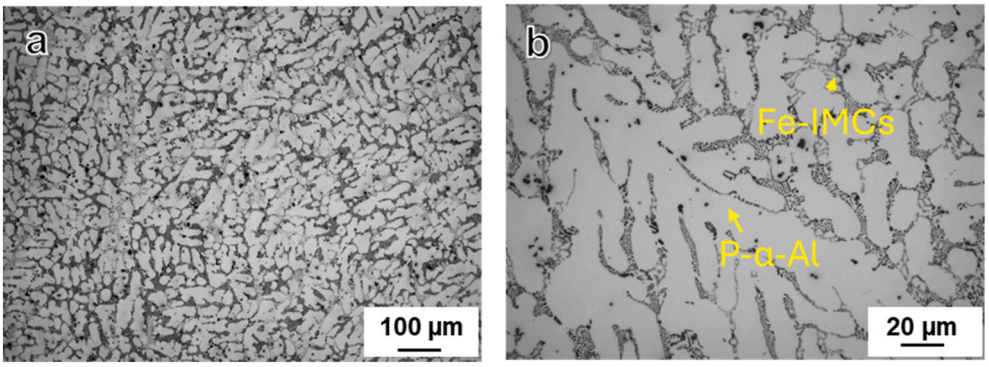

Fig. 3. Suppression of both primary and binary-eutectic (BE) Fe-IMCs via rapid solidification. Optical images of the as-cast Al–5Mg–2Si-0.7Mn-1.2Fe alloy cast at 40 K/s from 720 °C (Condition 10#): (a) Low-magnification view showing suppression of primary Fe-IMCs, with the microstructure consisting of primary α-Al and eutectic structures; (b) Higher-magnification view showing elongated primary α-Al and inter-dendritic SPPs (Fe-IMCs and Mg_2Si).

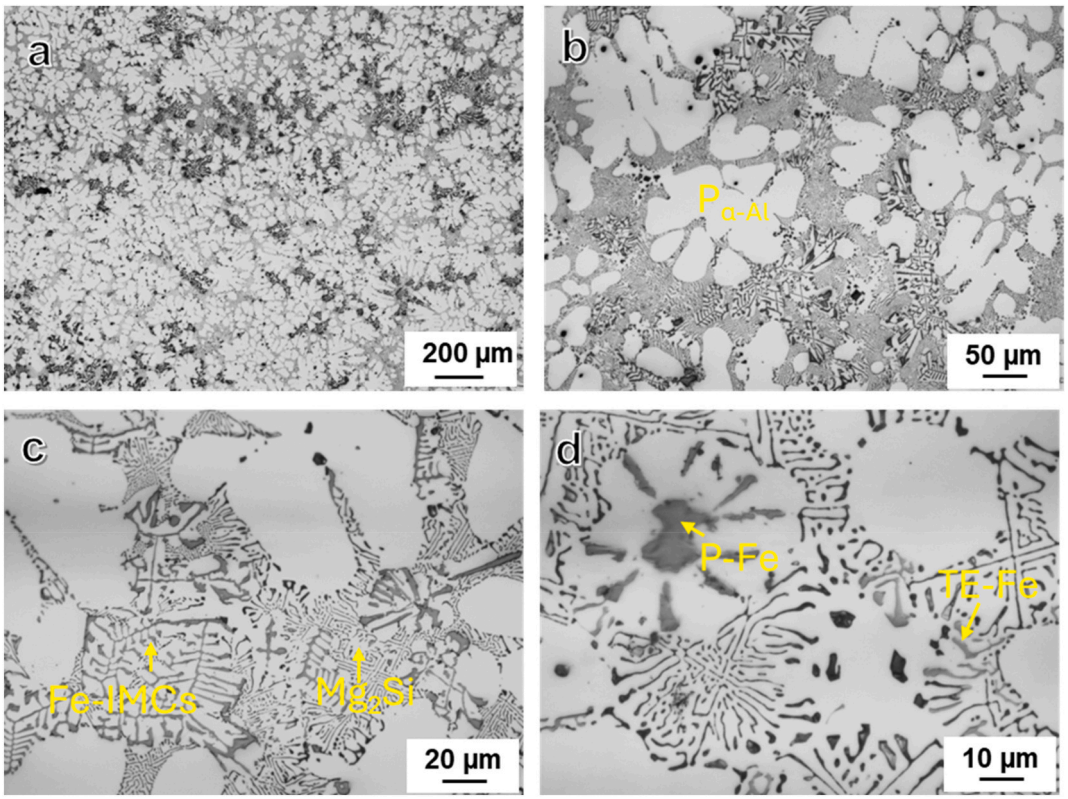

Fig. 4. Suppression of primary Fe-IMCs at a pouring temperature slightly below the eutectic point. As-cast microstructure of Al–5Mg–2Si-0.7Mn-1.2Fe alloy cast at 3.5 K/s and 620 °C (below the eutectic point of 620.5 °C, Condition 6#): (a) Microstructure showing primary α-Al and inter-dendritic SPPs, with Fe-IMCs exhibiting Chinese-script morphology sized 50–200 μm (longest 2D length); (b) Small α-Al grains (~200 μm) with inter-dendritic Fe-IMCs and Mg_2Si; (c) High-magnification image highlighting Chinese-script morphologies of Fe-IMCs and Mg_2Si, with Fe-IMC spacing of 5.5 ± 1 μm and Mg_2Si spacing of 1.6 ± 0.4 μm; (d) Rare primary Fe-IMCs within α-Al grains, associated with needle- or plate-like β-Fe-IMCs and some ternary Fe-IMCs linked to Mg_2Si particles.

μm, distributed within α-Al grains and inter-dendritic eutectic regions (Fig. 5a). Occasionally, some larger Fe-IMCs (~50 μm) particles can be observed. Deep-etched SEM-BSD imaging (Fig. 5b) reveals the 3D morphology of these primary Fe-IMCs as cuboid or parallelepiped shapes, while Fig. 5c shows their connection to surrounding Chinese-script BE-Fe-IMCs, which in turn are also linked to Mg_2Si within the eutectic structure. Additional observations at the same pouring temperature (Fig. 5d–f) highlight slightly refined Fe-IMCs (P2) with a size range of 5–30 μm, along with a few larger Fe-IMCs (P1) when cast at 630 °C. SEM-BSD imaging (Fig. 5e) contrasts the large P1 Fe-IMCs with smaller P2 Fe-IMCs (~10 μm) interconnected with surrounding eutectic Fe-IMCs. Within individual α-Al dendrites (Fig. 5f), P2–Fe particles are embedded along with their surrounding eutectic Fe-IMCs, illustrating the complex nucleation and growth relationships under these pouring conditions. Table 4 compares the compositions of P1–Fe and P2–Fe. P1–Fe contains lower Fe and Mn than P2–Fe, likely influenced by the composition of pre-existing Fe-rich intermetallic θ-$Al_{13}M_4$ or Al_6(Fe, Mn)) and the surrounding liquid. In contrast, P2–Fe forms directly by nucleation from the liquid melt, allowing it to achieve the required equilibrium composition directly from the melt. In addition, P1–Fe solidified at higher temperatures, resulting in larger particles size due to the longer growth time, Table 4.

The nature and morphology of α-Al_{15}(Fe,Mn)$_3Si_2$ particles in Al–5Mg–2Si-0.7Mn-1.2Fe alloy solidified from 630 °C (Fig. 5d) was investigated and presented in Fig. 6. High-resolution TEM imaging (Fig. 6a) shows the (110) faceted surface of α-Al_{15}(Fe,Mn)$_3Si_2$ when viewed along the [110] direction, highlighting its well-defined crystallography. SEM images reveal the three-dimensional morphology of these particles following solidification at 3.5 K/s from 630 °C. Fig. 6b shows a cubic particle with a (100) faceted surface, while Fig. 6c displays a parallelepiped morphology with (110) facets. Although the morphologies of the P2–Fe particles differ, their compositions averaged over at least 20 particles are nearly identical. SEM-EDS analysis shows that the cubic P2–Fe particles contain 16.93 ± 0.51 wt% Fe, 14.76 ± 0.46 wt% Mn, and 4.55 ± 0.15 wt% Si on average, while the parallelepiped P2–Fe particles contain 17.57 ± 0.60 wt% Fe, 15.65 ± 0.55 wt% Mn, and 3.89 ± 0.32 wt% Si. Fig. 6d demonstrates twinning within a single particle, showing multiple faceted surfaces.

Further investigation using EBSD revealed the twinning behaviour of α-Al_{15}(Fe,Mn)$_3Si_2$ in primary particles of the Al–5Mg–2Si-0.7Mn-1.2Fe alloy under Cooling Condition 2#. Fig. 7a shows the image quality (IQ) map, highlighting the well-defined crystallographic features of the particles. The corresponding phase map (Fig. 7b) confirms the presence of α-Al_{15}(Fe,Mn)$_3Si_2$, while the inverse pole figure (IPF) map (Fig. 7c) clearly illustrates the twinned regions within the primary particles. These EBSD results demonstrate that twinning is a characteristic feature of α-Al_{15}(Fe,Mn)$_3Si_2$, which may influence its faceted surface and morphology shown in Fig. 6.

3.4. Formation mechanism of P1–Fe and P2–Fe

To understand the formation mechanism of two different size range of α-Al_{15}(Fe,Mn)$_3Si_2$, the samples collected from the slow cooled sedimentation was examined using OM, SEM and CT, and TEM.

The slow-cooled samples prepared under casting condition #8 (cooled from 720 °C at 0.02 K/s) exhibit clearly distinguishable phase-zoned regions, as shown in Fig. 8. A small number of large primary Fe-IMCs (Fig. 8d) are observed at the bottom of the sample, where they connect to a region enriched in blocky Fe-IMCs (BE-Fe, Fig. 8c). Above this zone lies the TE-Fe region (Fig. 8b), consisting primarily of α-Al

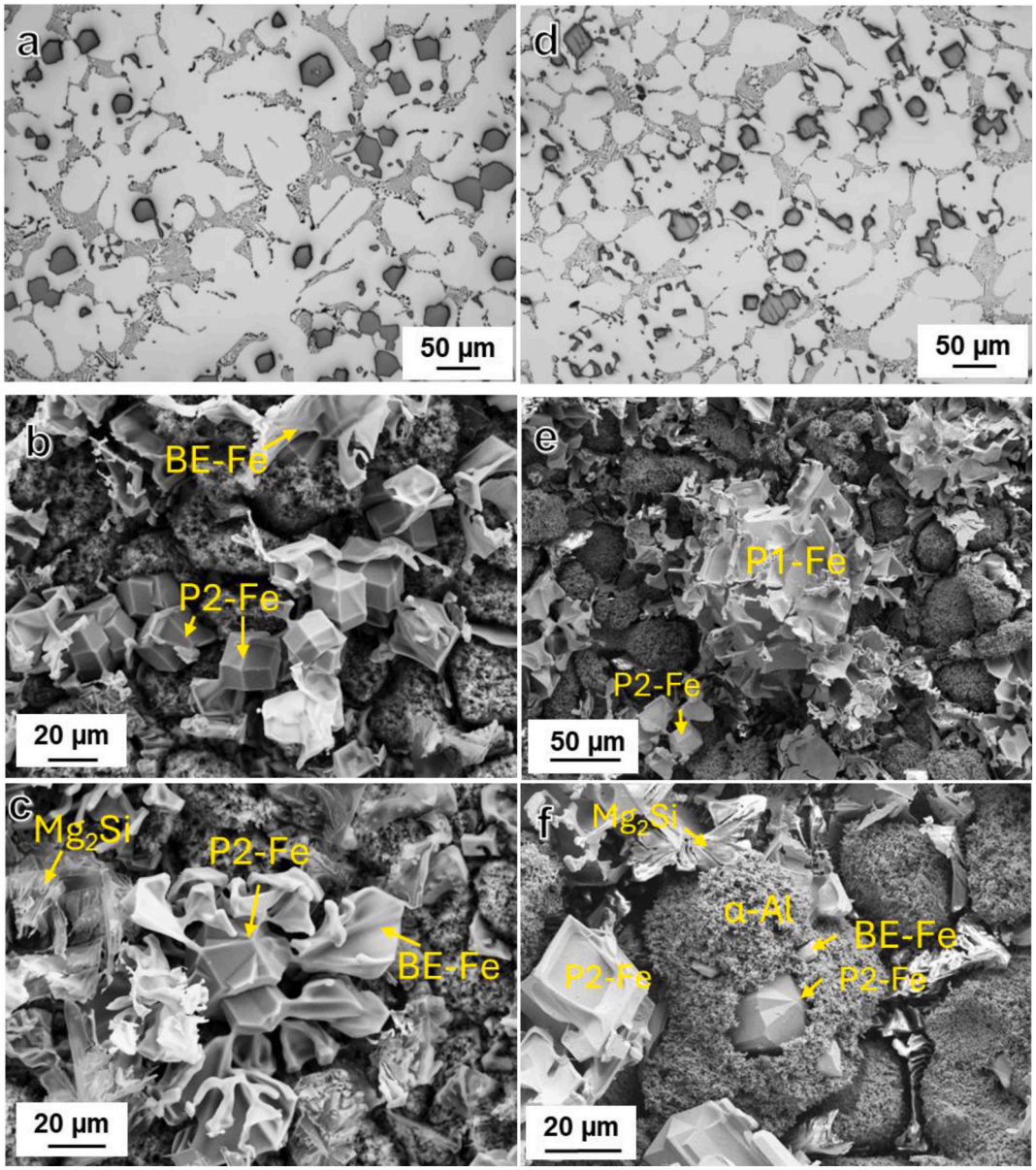

Fig. 5. Stimulated nucleation of Fe-IMCs via pouring temperature between the eutectic and liquidus points. As-cast microstructure of Al–5Mg–2Si-0.7Mn-1.2Fe alloy casted at 3.5 K/s: (a–c) cast at 650 °C ($T_E < T_p < T_L$) (condition 4#): (a) Increased primary Fe-IMC particles, 15–30 μm, located within α-Al grains and inter-dendritic eutectic; (b) SEM-BSD image showing deep-etched 3D morphology of primary Fe-IMCs with cuboid or parallelohedron shapes; (c) SEM-BSD image showing primary Fe-IMCs connected with surrounding Chinese-script BE Fe-IMCs, which are further connected to Mg_2Si in the eutectic structure. (d–f) casted at 630 °C ($T_E < T_p < T_L$) (condition 5#): (d) OM image showing slightly refined P1 Fe-IMCs (5–30 μm) and a few larger P1 particles; (e) SEM-BSD comparison of large P1 Fe-IMCs (~100 μm) and small P2 Fe (~10 μm) connected to surrounding eutectic Fe-IMCs; (f) SEM-BSD image showing P1–Fe embedded within a single Al dendrite, surrounded by eutectic Fe-IMCs.

Table 4
Composition (SEM-EDS) and size range of Fe-IMCs.

	Al (at.%)	Fe	Mn	Si	Size
P1–Fe (peritectic)	75.96	11.18	7.35	5.52	30–100 μm
P2–Fe	63.38	17.25	15.2	4.22	<30 μm

together with TE structures (α-Al + Fe-IMCs + Mg_2Si). The top region of the sample contains extensive oxide films associated with Fe-IMCs and visible porosity.

The compositions of these distinct regions were examined by SEM-EDS area mapping, with mapping areas selected to fully cover the major features of each zone, for example, a 2 × 1 mm^2 area for the primary Fe-IMC region, and 2 × 2 mm^2 areas for both the BE-Fe and TE-Fe regions. The results show that the sedimented primary Fe-IMCs (P1) area at the bottom exhibit a composition of approximately (Fe + Mn) ≈ 5 wt%. Above this zone, the BE-rich region contains approximately (Fe + Mn) ≈ 0.8 wt%, while the TE-Fe region remains relatively clean, with (Fe + Mn) ≈ 0.5 wt%.

No small size P2–Fe was observed at this solidification condition (8#). CT scanning further revealed that the P1 α-$Al_{15}(Fe,Mn)_3Si_2$ were formed via phase transformation from central θ-$Al_{13}Fe_4$ particles rather than by direct nucleation on oxides. The details of the phase transformation mechanism have been reported in our previous paper [19]. Three-dimensional imaging shows the morphology of the sedimented P1 Fe-IMCs at the interface between the bottom and middle BE zones, while internal plate-like θ-$Al_{13}Fe_4$ can be observed within the α-$Al_{15}(Fe,Mn)_3Si_2$ particles. These results indicate that the primary Fe-IMCs grow

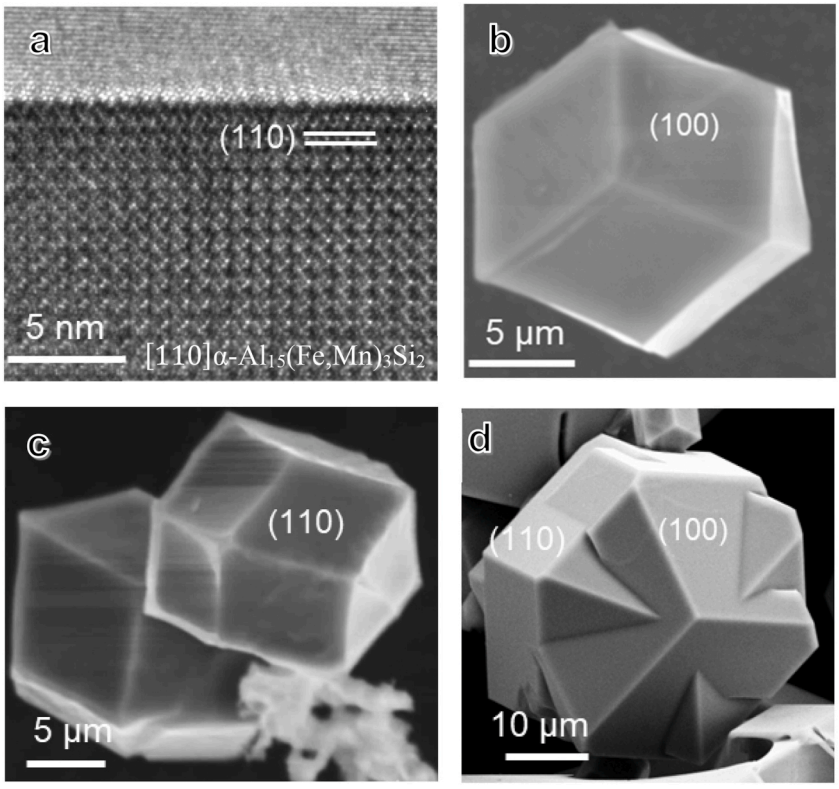

Fig. 6. Morphology and crystallography of the α-$Al_{15}(Fe,Mn)_3Si_2$: (a) High resolution (HR)-TEM image showing the (110) faceted fact of the α-$Al_{15}(Fe,Mn)_3Si_2$ viewed along the [110] direction; (b–d) SEM images showing 3D morphologies of α-$Al_{15}(Fe,Mn)_3Si_2$ particles from Al–5Mg–2Si-0.7Mn-1.2Fe alloy cooled at 3.5 K/s from 630 °C (condition 5#); (b) cubic particle with (100) faceted surface; (c) parallelepiped particle with (110) faceted surface; (d) twinned particle exhibiting multiple faceted surfaces.

via phase transformation, and their low sedimentation efficiency is influenced by both their formation mechanism and the surrounding microstructure.

A special technology was developed to enhance sedimentation efficiency by stimulating the formation of primary Fe-IMCs, based on the experimental findings presented in Figs. 1–5. In this process, the melt was first cooled to 630 °C that is close to the temperature of T_{fcc} (620.5 °C), reheated above the liquidus (670 °C), and then subjected to casting at 3.5 K/s and sedimentation (0.02 K/s). Fig. 9 demonstrates that stimulating primary Fe-IMC formation remarkedly improved Fe removal efficiency in the Al–5Mg–2Si-0.7Mn-1.2Fe alloy. Under Condition 7# (three-stage solidification: 720-630-670 °C), optical imaging (Fig. 9a and b) revealed a few large P1 α-Fe particles alongside numerous P2 α-Fe particles. These particles were located either within α-Al grains or along grain boundaries, with a clear reduction in the volume fraction of the BE-α-$Al_{15}(Fe,Mn)_3Si_2$ compared with earlier observations (Fig. 2a). Furthermore, by applying a four-stage solidification strategy (720-630-670 °C followed by slow cooling to 200 °C), primary Fe-IMCs were successfully collected via sedimentation, Fig. 9c. Fig. 9c shows the 2D morphology of compact Fe-IMC particles, while SEM imaging (Fig. 9d) reveals their 3D structures, with P1 and P2 particles displaying cubic or parallelepiped shapes, in contrast to those collected previously (Fig. 8a). After sedimentation, the (Fe + Mn) content at the cleaned area can reach a new low level of 0.3 wt% in this case. The composition measurement is followed the previous one on a 2 × 2 mm^2 areas in the target area.

The formation mechanism of small size P2–Fe was investigated via investigating the heterogeneous nucleation mechanism. Fig. 10 presents a first time TEM observations providing direct evidence of heterogeneous nucleation of α-$Al_{15}(Fe,Mn)_3Si_2$ on native $MgAl_2O_4$ particles. In the bright-field TEM image (Fig. 10a), $MgAl_2O_4$ particles are seen embedded within the α-$Al_{15}(Fe,Mn)_3Si_2$ particle. High-resolution TEM (Fig. 10b) reveals the distinct interface between the $MgAl_2O_4$ and α-$Al_{15}(Fe,Mn)_3Si_2$, indicating nucleation of the intermetallic on the oxide surface. Selected area electron diffraction (SAED) patterns confirm the crystallographic orientations: Fig. 10c shows α-$Al_{15}(Fe,Mn)_3Si_2$ along the [100] zone axis, Fig. 10d shows $MgAl_2O_4$ along [111], and Fig. 10e overlays both sets of SAED patterns, illustrating their orientation relationship:

$$(042)[100]\ \alpha\text{-}Al_{15}(Fe,Mn)_3Si_2\ //\ (02\bar{2})[111]\ MgAl_2O_4.$$

The indexed SAED pattern in Fig. 10f further confirms the lattice alignment between α-$Al_{15}(Fe,Mn)_3Si_2$ and $MgAl_2O_4$, providing conclusive evidence that the oxide particles serve as nucleation sites for the intermetallic phase. It should be noted that the majority of $MgAl_2O_4$ particles observed from the collected oxides typically exhibit {111} faceted surfaces with parallelepiped morphologies [23]. However, the particle observed here is hexagonal with a {110} faceted surface, which may also reflect the increased difficulty in nucleating α-$Al_{15}(Fe,Mn)_3Si_2$.

4. Discussion

4.1. Nucleation difficulty of Fe-IMCs

The present study reveals the complex solidification behaviour of Fe-IMCs within a broad freezing range of ~50 K for primary α-$Al_{15}(Fe,Mn)_3Si_2$. This wide interval provides space for compression effects, stimulation, and phase competition among multiple Fe-IMCs and α-Al. As a result, the alloy exhibits significant variations in phases volume fraction, leading to changes in the leading solidification phase, as well as in the morphology and size distribution of Fe-rich secondary phase particles (SPPs).

The coexistence of large P1 and smaller P2 α-Fe particles has been reported under special casting conditions such as HPDC [24]. However, the underlying mechanism for their concurrent formation has remained

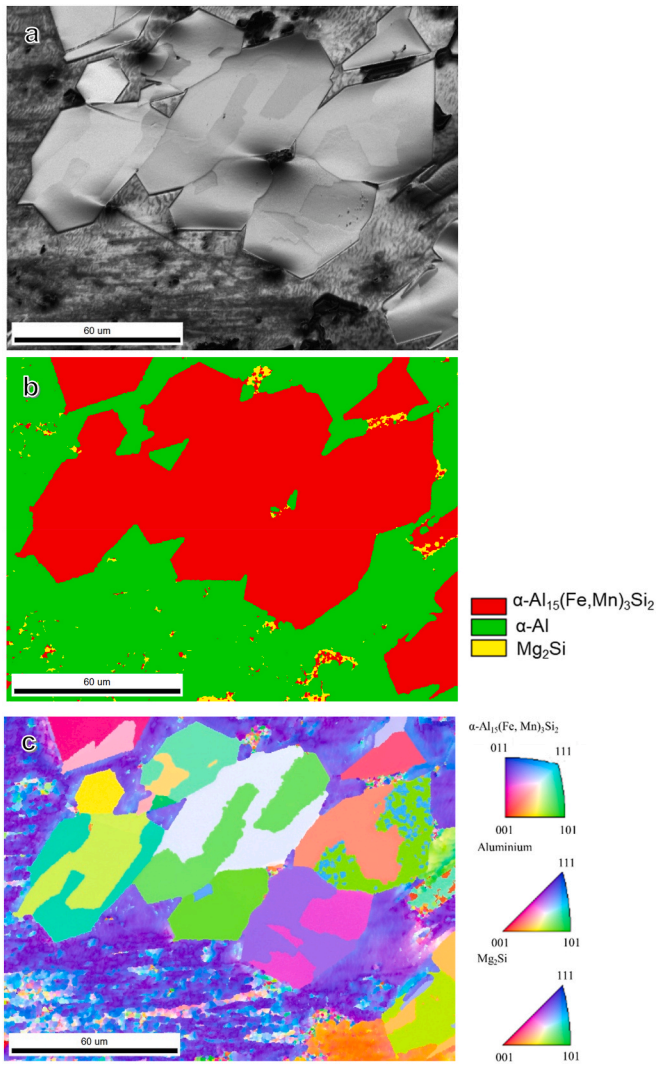

Fig. 7. EBSD maps showing twinning in α-$Al_{15}(Fe,Mn)_3Si_2$ within settled primary particles of Al–5Mg–2Si-0.7Mn-1.2Fe alloy cooled under condition 2. (a) IQ map; (b) phase map; and (c) IPF map.

elusive. The present work provides direct evidence, for the first time, clarifying their origin. Large P1 α-Fe particles are shown to result from phase transformation of other metastable Fe-IMCs (θ-$Al_{13}Fe_4$), while small P2 α-Fe particles nucleate directly from the melt. Because α-$Al_{15}(Fe,Mn)_3Si_2$ suffers from high nucleation difficulty [14], metastable Fe-IMCs such as θ-$Al_{13}Fe_4$ form preferentially at earlier stages of solidification, subsequently transforming into α-Fe. This explains the dual size distribution observed under tailored thermal conditions (Fig. 9).

The nucleation of Fe-IMCs is strongly constrained by their complex crystallography and weak compatibility with the Al matrix, resulting in high nucleation barriers. Structurally, their complex unit cell configurations, such as that of α-$Al_{15}(Fe,Mn)_3Si_2$, increase interfacial energy, while the large lattice mismatch with α-Al lowers heterogeneous nucleation potency, and native oxides in the melt offer poor substrates for nucleation. From a compositional perspective, the requirement for multiple solute elements (Fe, Mn, Si) reduces the chemical driving force, the low latent heat of formation provides limited thermal feedback, and slow solute diffusion hinders the growth of critical nuclei. These combined structural and compositional constraints explain why metastable Fe-IMCs such as θ-$Al_{13}Fe_4$ often nucleate first and subsequently transform into more stable α-Fe phases.

Therefore, nucleation difficulty is the primary factor responsible for the low sedimentation efficiency and the limited Fe removal efficiency (typically no lower than 0.7 wt%). It also drives the complex phase competition among different Fe-IMCs, such as the equilibrium α-$Al_{15}(Fe,Mn)_3Si_2$ phase and the non-equilibrium θ-$Al_{13}Fe_4$ phase predicted by phase diagrams. This explains why traditional thermodynamic calculations struggle to accurately predict Fe-IMC formation, leading to challenges in alloy design. Nucleation difficulty sets the kinetic barrier, and phase competition determines which phases can form under given conditions, making Fe-IMC formation extremely sensitive to cooling rate and pouring temperature.

This study demonstrates a practical approach to simulate the formation of primary Fe-IMCs, enabling effective Fe removal down to a new low level of 0.3 wt%. Conversely, we also explored an alternative method involving casting at ultra-low temperatures (e.g., 620 °C, below the eutectic point of 620.5 °C, Fig. 4) or under ultra-high cooling rates (40 K/s, Fig. 3). Under these conditions, most Fe-IMCs were forced into the eutectic regions, resulting in significantly refined microstructures compared to conventional casting (Fig. 2). Further studies are needed to optimize and implement this practical approach, taking into account factors such as castability, porosity, and other processing constraints.

4.2. *Coupling of nucleation difficulty with thermodynamic and kinetic effects under different casting conditions*

The experimental results (Figs. 1–5) reveal pronounced phase competition and a strong sensitivity of Fe-intermetallic compound (Fe-IMC) formation to casting parameters, particularly pouring temperature and cooling rate. This complicated phase competition was previously report and discussed solely based on the thermodynamic effects [25–28]. In this paper, a systematic discussion shows that the solidification behaviour originates fundamentally from the high nucleation difficulty of Fe-IMCs, which amplifies the sensitivity of Fe-IMC formation to thermodynamic and kinetic factors controlled by casting parameters. The schematic evolution map presented in Fig. 11 summarizes the interrelationships among the liquidus, nucleation temperatures of various Fe-IMCs and α-Al, pouring temperature, cooling rate, and the resulting solidification sequence.

From a thermodynamic standpoint, the driving force for Fe-IMC nucleation increases with increasing undercooling and solute supersaturation. Lower pouring temperatures and progressive Fe enrichment in the remaining liquid during solidification reduce the Gibbs free energy for Fe-IMC formation, thereby lowering the critical nucleation barrier. However, due to the high intrinsic nucleation difficulty of Fe-IMCs including both structural and compositional templating, a substantial thermodynamic driving force is often required before nucleation can occur. Pouring temperature directly determines the initial degree of undercooling with respect to the liquidus temperature at the onset of solidification. A lower pouring temperature results in a larger initial undercooling, which increases the thermodynamic driving force for nucleation by enlarging the free-energy difference between the liquid and solid phases. In contrast, a higher pouring temperature reduces the initial undercooling and delays the onset of nucleation. A rapid cooling rate increases the nucleation undercooling but simultaneously reduces atomic diffusion.

The recent fundamental research on the nucleation of Fe-IMCs revealed that the nucleation of Fe-IMCs is not solely governed the classical nucleation barrier associated with interfacial energy and volumetric free energy change, it is also strongly constrained by compositional templating effects [14], which require the simultaneous arrangement of multiple alloying elements at specific atomic sites during the pre-nucleation and nucleation stages [29]. Such compositional templating imposes additional kinetic constraints on nucleation, as the formation of a chemically ordered nucleus demands local enrichment and precise atomic configurations.

This requirement is particularly restrictive for elements such as Fe and Mn, which exhibit relatively low diffusion coefficients compare to

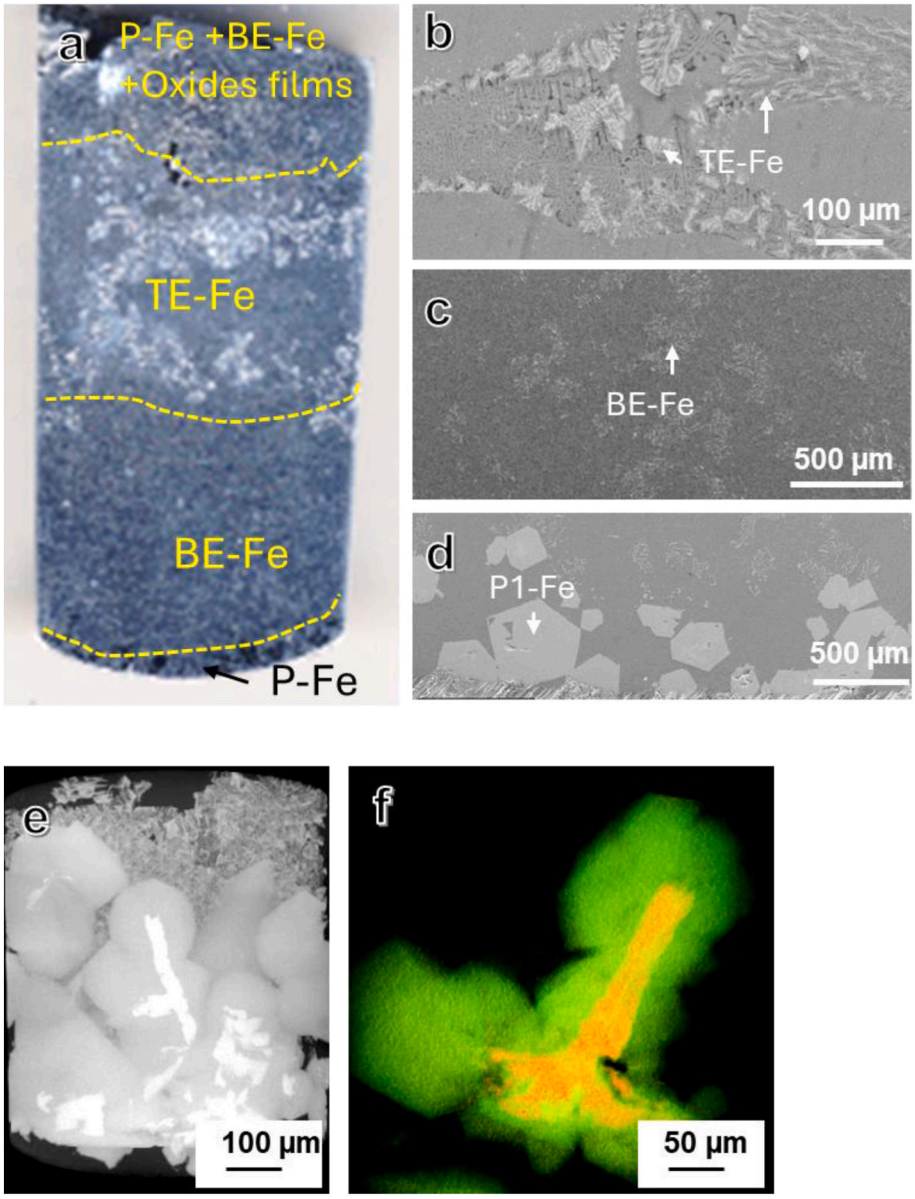

Fig. 8. Formation mechanism of P1 Fe-IMCs and their low sedimentation efficiency. (a) Small sample slowly cooled in the crucible (0.02 K/s) from 720 °C (Condition 8#), showing: (b) a clean area with (Fe + Mn) = 0.5 wt%, (c) a binary eutectic-rich area with (Fe + Mn) = 0.8 wt%, and (d) sedimented primary Fe-IMCs (P1) with (Fe + Mn) = 5 wt%. (e) CT scanning images further reveal that these P1 α-$Al_{15}(Fe,Mn)_3Si_2$ particles are phase-transformed from central θ-$Al_{13}Fe_4$ rather than nucleating directly on oxides. Insets: (1) 3D morphology of sedimented P1 Fe-IMCs at the interface between the bottom and middle BE area; (2) internal plate-like θ-$Al_{13}Fe_4$ within observed α-$Al_{15}(Fe,Mn)_3Si_2$ particles.

the other elements such as Mg and Si in liquid aluminium [15]. The limited atomic mobility of these elements significantly prolongs the time required to establish the necessary local compositional fluctuations, thereby increasing the effective nucleation difficulty. Consequently, even when a sufficient thermodynamic driving force is available, the nucleation of Fe-IMCs may remain kinetically suppressed.

Furthermore, the complex crystal structures of Fe-IMCs, characterized by large unit cells and multiple inequivalent atomic sites, demand a higher degree of atomic ordering during nucleation. This structural complexity further elevates the critical undercooling required for stable nucleus formation. As a result, Fe-IMC nucleation typically occurs only under conditions of substantial undercooling, prolonged diffusion time, or both, reinforcing the strong sensitivity of Fe-IMC formation to cooling rate and pouring temperature observed experimentally.

A few cases reported in this paper can be explained with the above discussion. At a cooling rate of 3.5 K/s with the pouring temperature above the liquidus, the thermodynamic driving force at early stages of solidification is insufficient to overcome the nucleation barrier of equilibrium α-$Al_{15}(Fe,Mn)_3Si_2$. As a result, its direct nucleation is suppressed. Instead, non-equilibrium Fe-IMCs with lower effective nucleation barriers, such as θ-$Al_{13}Fe_4$ and $Al_6(Fe,Mn)$, nucleate firstly. These phases subsequently transform into the equilibrium α-$Al_{15}(Fe,Mn)_3Si_2$ phase as solidification proceeds and solute redistribution continues. This sequence reflects a kinetically preferred pathway in which phases with lower ΔG* nucleate under limited undercooling, even if they are not thermodynamically most stable.

When the alloy is cast at the same cooling rate but with the pouring temperature below the liquidus and above T_{fcc} i.e., within the freezing range of primary α-$Al_{15}(Fe,Mn)_3Si_2$, two distinct formation pathways are activated. In addition to P1, which forms through transformation of non-equilibrium Fe-IMCs, the second particles (P2) of α-$Al_{15}(Fe,Mn)_3Si_2$ nucleate directly on native oxide substrates at lower temperature. The

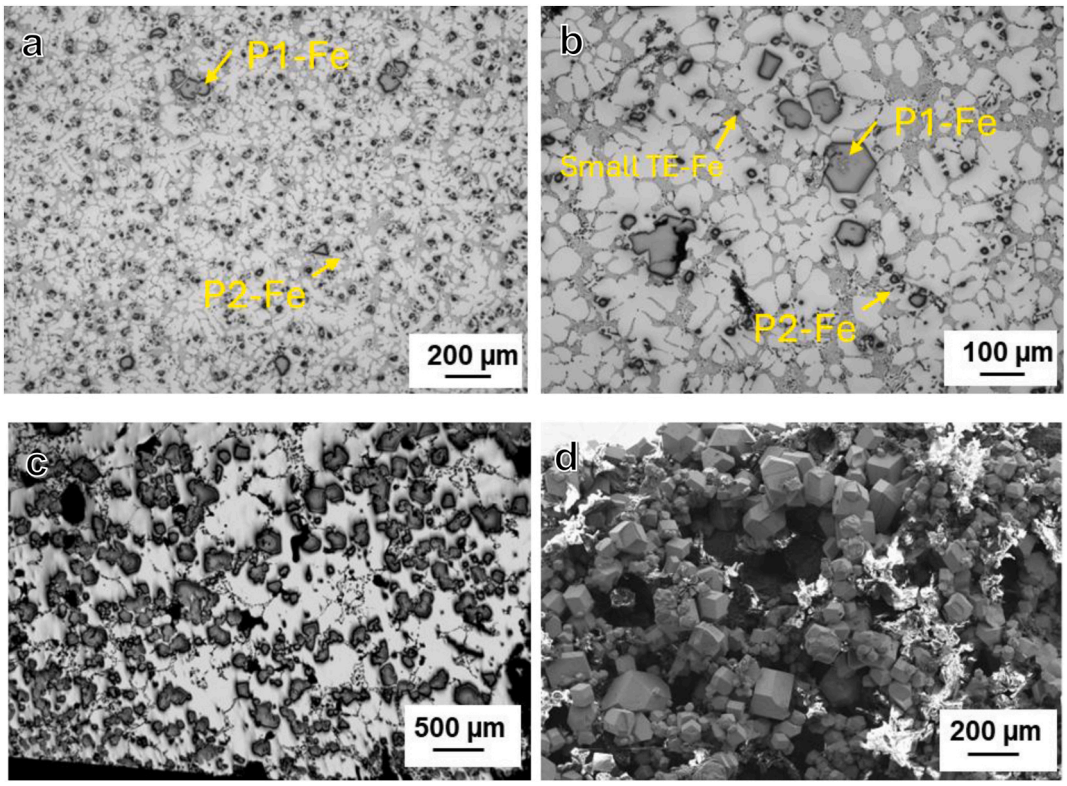

Fig. 9. Stimulation of primary Fe-IMC formation significantly enhances Fe removal efficiency. (a–b) Optical images of Al–5Mg–2Si-0.7Mn-1.2Fe alloy cast under Condition 7# (three-stage solidification: 720–630–670 °C): (a) showing a few P1 α-Fe and numerous P2 α-Fe particles; (b) distribution of P1 and P2 α-Fe particles within α-Al grains or along grain boundaries, with a marked reduction in the volume fraction of binary eutectic (BE) α-$Al_{15}(Fe,Mn)_3Si_2$ compared to Fig. 2a. (c–d) Primary Fe-IMCs collected via sedimentation using a four-stage solidification strategy (720–630–670–20 °C): (c) optical image showing 2D morphology of compact Fe-IMC particles; (d) SEM image revealing 3D morphology of collected P1 and P2 particles with cubic or parallelepiped shapes.

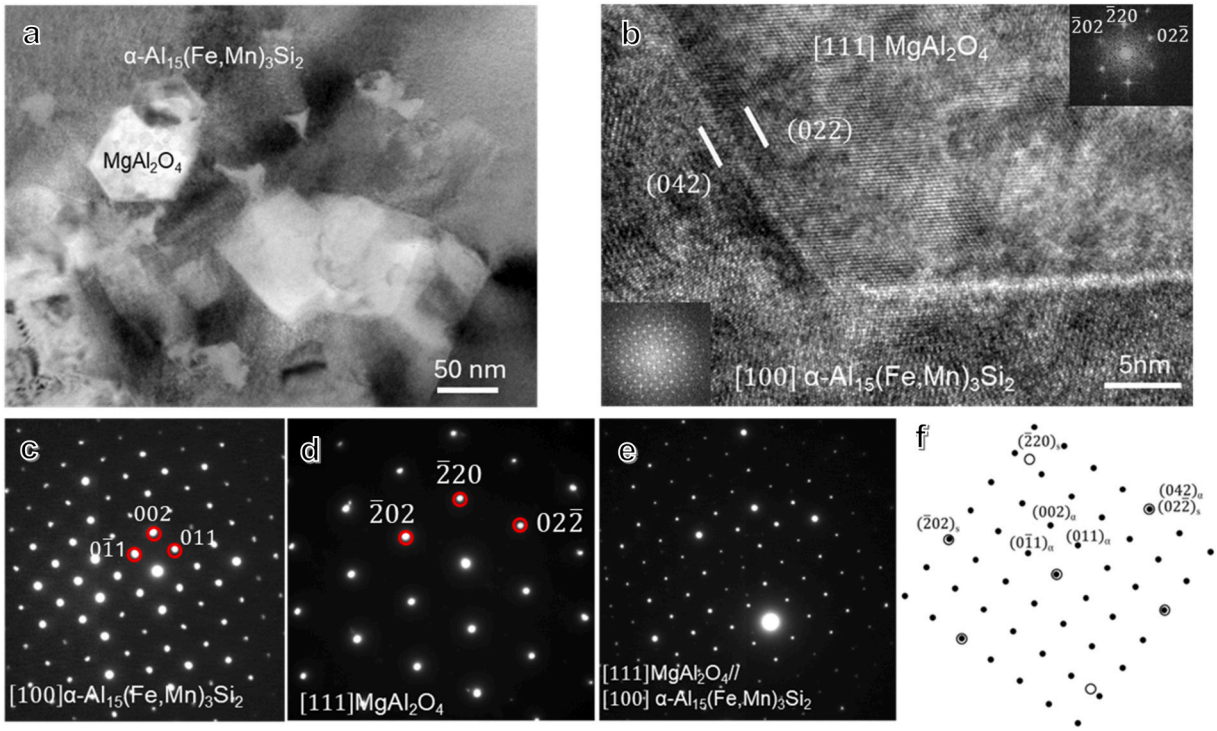

Fig. 10. TEM observations providing direct evidence of heterogeneous nucleation of α-$Al_{15}(Fe,Mn)_3Si_2$ on native $MgAl_2O_4$. (a) Bright field (BF)-TEM image showing $MgAl_2O_4$ particles embedded within α-$Al_{15}(Fe,Mn)_3Si_2$; (b) High resolution (HR)-TEM image of interface between $MgAl_2O_4$ and α-$Al_{15}(Fe,Mn)_3Si_2$; (c) SAED pattern of α-$Al_{15}(Fe,Mn)_3Si_2$ along the [100] zone axis; (d) SAED pattern of $MgAl_2O_4$ along [111] zone axis; (e) Combined SAED patterns of both α-$Al_{15}(Fe,Mn)_3Si_2$ and $MgAl_2O_4$; (f) Indexed SAED patterns corresponding to (d).

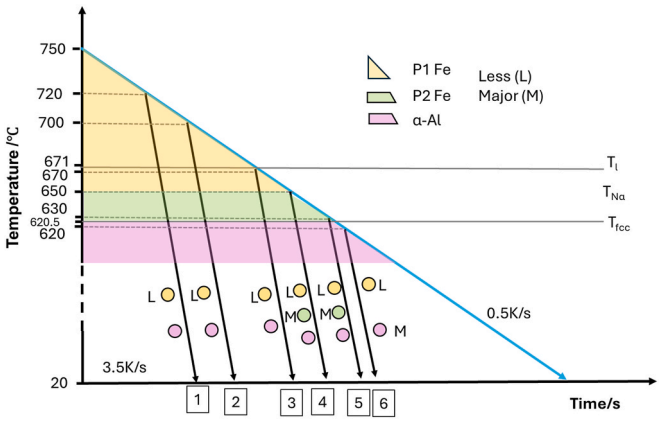

Fig. 11. Schematic illustrating the relationships among the liquidus, nucleation temperatures of different Fe-IMCs and α-Al, pouring temperature, cooling rate, and the solidification sequence.

appearance of P2 indicates that only after sufficient undercooling does the thermodynamic driving force become large enough to overcome the high heterogeneous nucleation barrier of α-$Al_{15}(Fe,Mn)_3Si_2$, even in the presence of potent nucleation sites. This observation highlights the critical role of undercooling in enabling direct nucleation of equilibrium Fe-IMCs.

In contrast, when the alloy is continuously slow-cooled below the freezing range of primary α-$Al_{15}(Fe,Mn)_3Si_2$ without quenching, as in conventional mould casting, P2 is rarely observed. Under these conditions, the undercooling develops gradually and is not sustained, allowing early nuclei to redissolve and reducing the effective thermodynamic driving force for further nucleation. For example, under casting condition 8 (slow furnace cooling), only the transformed P1 phase is detected (Fig. 8). This demonstrates that continuous and sustained undercooling is essential not only to initiate nucleation but also to preserve nuclei against redissolution and to trap Fe and Mn solutes that would otherwise remain dissolved during slower cooling.

The kinetic limitations further modulate this behaviour. The diffusion coefficients of Fe and Mn in the liquid are relatively low and decrease rapidly with temperature according to Ref. [30]:

$$D = D_0 \exp\left(-\frac{Q}{RT}\right)$$

At extremely fast cooling rates, diffusion times become insufficient to support solute redistribution and interface rearrangement, further suppressing the nucleation of primary Fe-IMCs, as observed in Fig. 3. While mould quenching provides more efficient heat extraction than furnace cooling and enhances both the magnitude and duration of undercooling, excessively rapid cooling imposes severe kinetic constraints that can outweigh the thermodynamic driving force.

These competing effects of undercooling and atomic diffusion, governed by the underlying thermodynamic and kinetic factors and closely linked to casting parameters such as pouring temperature and cooling rate, create a narrow processing window for Fe-IMC formation, as illustrated in Fig. 11, which exists only below the liquidus temperature.

From an industrial perspective, a clear strategy is therefore needed to expand the formation window of equilibrium α-Fe phases. This can be achieved either by enhancing effective diffusion to support compositional templating or by reducing the kinetic barriers to nucleation. Our recent publication demonstrates one such approach, in which compositional templating is introduced directly on nucleation substrates to stimulate the formation of α-Fe [14].

5. Conclusions

1) The formation of primary α-$Al_{15}(Fe,Mn)_3Si_2$ is readily suppressed under conventional casting conditions (cooling rate of ~3.5 K/s and pouring temperature 50 K above the calculated liquidus). Under these conditions, its volume fraction is significantly lower than that predicted by thermodynamic calculations.
2) The freezing range of primary α-$Al_{15}(Fe,Mn)_3Si_2$ in the studied alloy is up to several tens of kelvins. During solidification, non-equilibrium Fe-rich intermetallic (Fe-IMCs), including Al_6(Fe, Mn) and θ-$Al_{13}Fe_4$, compete with the equilibrium α-$Al_{15}(Fe,Mn)_3Si_2$ phase for nucleation.
3) Rapid solidification (≈40 K/s) or a substantially reduced pouring temperature (closed to the formation temperature of α-Al, 620.5 °C) effectively suppresses the formation of primary α-$Al_{15}(Fe,Mn)_3Si_2$, leading instead to a higher overall volume fraction of Fe-IMCs within the secondary primary particles.
4) In contrast, multiple-stage casting routes significantly promote the formation of primary α-$Al_{15}(Fe,Mn)_3Si_2$. This enhancement reduces the volume fraction of SPP-associated Fe-IMCs and improves the overall Fe removal efficiency.
5) The primary α-$Al_{15}(Fe,Mn)_3Si_2$ phase exhibits faceted morphologies bounded by {110} and {100} planes, appearing as parallelepiped or cubic particles. These particles are naturally twinned.
6) Large P1–Fe particles were identified as result of phase transformation from non-equilibrium θ-$Al_{13}Fe_4$. In contrast, smaller P2–Fe particles nucleate heterogeneously on native spinel $MgAl_2O_4$ particles.
7) The orientation relationship between P2–Fe and $MgAl_2O_4$ is identified as: $(042)[100]$ α-$Al_{15}(Fe,Mn)_3Si_2$//$(02\bar{2})[111]$ $MgAl_2O_4$.

Declaration of competing interest

The authors declare that they have no known competing financial interests or personal relationships that could have appeared to influence the work reported in this paper.

Acknowledgement

This work was financial supported by the EPSRC (UK) for under grant number EP/N007638/1 (Future Liquid Metal Engineering Hub) and Brunel University of London BRIEF award (11937131).

References

[1] IRENA 2025. Reaching Zero with renewables: aluminium industry. 2025.
[2] Yi X, Lu Y, He G. Aluminum demand and low carbon development scenarios for major countries by 2050. J Clean Prod 2024;475:143647.
[3] Niu Z, Que Z, Patel JB, Fan Z. Assessment and improvement of melt quality of recycled secondary A357 alloy by application of the High shear melt conditioning (HSMC) technology. Crystal 2024;14(12):1044.
[4] Yang B, Friedrich S, Friedrich B. Advances in non-metallic inclusion removal from aluminum melts towards cleaner and higher-performance materials. J Mater Sci 2025;60:12291–314.
[5] Wu J, Djavanroodi F, Gode C, Attarilar S, Ebrahimi M. Melt refining and purification processes in Al alloys: a comprehensive study. Mater Res Express 2022; 9:032001.
[6] Gaustad G, Olivetti E, Kirchain R. Improving aluminum recycling: a survey of sorting and impurity removal technologies. Resour Conserv Recycl 2012;58:79–87.
[7] Fanconi MMV, Fernández-Marcote IG, Ruiz-Bustinza Íñigo. The challenge of impurities (Fe, si) to recycling in the rolled aluminum industry in the coming years in relation to their influence on ultimate tensile strength. Metals 2023;13(12): 2014.
[8] Zhang Y, Lei Y, Ren Y, Ma W. Removal of Fe impurities from Al alloy scraps by electromagnetic directional solidification combined with Si addition. J Mater Res Technol 2023;26:8738–47.
[9] Lazaro-Nebreda J, Patel JB, Al-Helal K, Gao F, Stone I, Chang ITH, Scamans GM, Fan Z. De-Ironing of aluminium alloy melts by high shear melt conditioning technology: an overview. Metals 2022;12(10):1579.
[10] Polmear I, et al. In: Light alloys – metallurgy of the light metals. 5th. Elsevier; 2017.

[11] Raabe D, Ponge D, Uggowitzer PJ, et al. Making sustainable aluminum by recycling scrap: the science of "dirty" alloys. Prog Mater Sci 2022;128:100947.
[12] Raabe D. The materials science behind sustainable metals and alloys. Chem Rev 2023;123(5):2436.
[13] Kleykamp H, Glasbrenner H. Thermodynamic properties of solid Aluminium-Iron Alloys. Int J Mater Res 2021;88(3).
[14] Que Z, Wang Y, Fan Z, Hashimoto T, Zhou XR. Composition templating for heterogeneous nucleation of intermetallic compounds. Sci Rep 2024;14:8968.
[15] Du Y, Chang YA, Huang B, Gong W, Jin Z, Xu H, Yuan Z, Liu Y, He Y, Xie F-Y. Diffusion coefficients of some solutes in fcc and liquid Al: critical evaluation and correlation. Mater Sci Eng, A 2003;363(1–2):140–51.
[16] Que Z, Wang Y, Fan Z. Formation of the Fe-containing intermetallic compounds during solidification of Al-5Mg-2Si-0.7 Mn-1.1 Fe alloy. Metall Mater Trans 2018; 49(6):2173–81.
[17] Dhinakar A, Lu P-Y, Tang N-K, Chen J-K. Iron reduction in 356 secondary aluminum alloy by Mn and Cr addition for sediment separation. Int J Metalcast 2021;15:182–92.
[18] Huang Y, Li L, Wen J, Liu Y. Evolution behavior of Fe and Fe-rich phases in high-Fe concentration al-si-mg alloy with Mn, Cr, and Co alloyed. Mater Today Commun 2024;39:108753.
[19] Que Z, Mendis CL. Heterogeneous nucleation and phase transformation of Fe-rich intermetallic compounds in Al–Mg–Si alloys. J Alloys Compd 2020;836:155515.
[20] Que Z, Fang C, Fan Z. Nucleation competition and phase transformation mechanisms in recycled aluminium alloys: insights into θ-Al13Fe4, Al6(Fe, Mn) and α-Al15(Fe, Mn)3Si2. J Alloys Compd 2025:181130.
[21] Scheil E. Bemerkungen zur Schichtkristallbildung. Z Met 1942;34:70–2.
[22] Aluminium Association: standard Test procedure for aluminium alloy grain refiners: TP-1. 1987. Washington DC.
[23] Que Z, Wang Y, Mendis CL. Heterogeneous nucleation of α-Al on naturally formed MgAl2O4 particles during solidification of Al-Mg-Si-Fe-Mn alloys. Materialia 2020; 14:100900.
[24] Zhu X, Dong X, Blake P, Ji S. Improvement in as-cast strength of high pressure die-cast Al-Si-Cu-Mg alloys by synergistic effect of Q-$Al_5Cu_2Mg_8Si_6$ and θ-Al_2Cu phases. Mater Sci Eng, A 2021;802:140612.
[25] Verma A, Kumar S, Grant PS, O'Reilly KAQ. Influence of cooling rate on the Fe intermetallic formation in an AA6063 Al alloy. J Alloys Compd 2013;555(5): 274–82.
[26] Dutta B, Rettenmayr M. Effect of cooling rate on the solidification behaviour of Al-Fe-Si alloys. Mater Sci Eng 2000;283(1–2):218–24.
[27] Becker H, Bergh T, Vullum PE, Leineweber A, Li Y. Effect of Mn and cooling rates on α-, β-, and δ-Al-Fe-Si intermetallic phase formation in a secondary Al-Si alloy. Materialia 2019;5:100198.
[28] Shang S-L, Sun H, Pan B, Wang Y, Krajewski AM, Banu M, Li J, Liu Z-K. Sci Rep 2021;11:24251.
[29] Men H, Fang CM, Fan Z. Prenucleation at the Liquid/Substrate interface: an overview. Metals 2022;12(10):1704.
[30] Flemings MC. Solidification processing. Metall Trans A 1974;(5):2121–34.